



CHORUS

This is the accepted manuscript made available via CHORUS. The article has been published as:

Flow-induced buckling dynamics of sperm flagella

Manish Kumar, Derek M. Walkama, Jeffrey S. Guasto, and Arezoo M. Ardekani

Phys. Rev. E **100**, 063107 — Published 20 December 2019

DOI: [10.1103/PhysRevE.100.063107](https://doi.org/10.1103/PhysRevE.100.063107)

Flow-induced buckling dynamics of sperm flagella

Manish Kumar,¹ Derek M. Walkama,^{2,3} Jeffrey S. Guasto,² and Arezoo M. Ardekani¹

¹*Department of Mechanical Engineering, Purdue University,
585 Purdue Mall, West Lafayette, Indiana 47907 USA*

²*Department of Mechanical Engineering, Tufts University,
200 College Avenue, Medford, Massachusetts 02155, USA*

³*Department of Physics and Astronomy, Tufts University,
574 Boston Avenue, Medford, Massachusetts 02155, USA*

(Dated: November 14, 2019)

The swimming sperm of many external fertilizing marine organisms face complex fluid flows during their search for egg cells. Aided by chemotaxis, relatively weak flows are known to enhance sperm-egg fertilization rates through hydrodynamic guidance. However, strong flows have the potential to mechanically inhibit flagellar motility through elasto-hydrodynamic interactions - a phenomenon that remains poorly understood. Here, we explore the effects of flow on the buckling dynamics of sperm flagella in an extensional flow through detailed numerical simulations, which are informed by microfluidic experiments and high-speed imaging. Compressional fluid forces lead to rich buckling dynamics of the sperm flagellum beyond a critical dimensionless sperm number, Sp , which represents the ratio of viscous force to elastic force. For non-motile sperm, the maximum buckling curvature and the number of buckling locations, or buckling mode, increase with increasing sperm number. In contrast, motile sperm exhibit a local flagellar curvature due to the propagation of bending waves along the flagellum. In compressional flow, this preexisting curvature acts as a precursor for buckling, which enhances local curvature without creating new buckling modes and leads to asymmetric beating. However, in extensional flow, flagellar beating remains symmetric with a smaller head yawing amplitude due to tensile forces. The flagellar beating frequency also influences the maximum curvature of motile sperm by facilitating sperm reorientation relative to the compressional axis of the flow near stagnation points. These combined simulations and experiments directly illustrate the microscopic elasto-hydrodynamic mechanisms responsible for inhibiting flagellar motility in flow, and have possible implications for our understanding of external fertilization in dynamic marine systems.

I. INTRODUCTION

The sperm of both external and internal fertilizers migrate vast distances, spanning orders of magnitude in their body length ($\sim 50 \mu\text{m}$), through complex fluid flows to locate egg cells and complete the fertilization process. Several guidance mechanisms, including chemotaxis [1–4] in the immediate vicinity of the ovum and rheotaxis [5–8] far away from the ovum, are known to aid sperm navigation toward the egg. For external fertilizing marine organisms, mild ambient fluid flows - characterized by shear rates, $\leq 0.1 \text{ s}^{-1}$ - enhance the efficacy of these guidance mechanisms and increase fertilization rates beyond that of quiescent fluid [3, 9, 10]. However, strong flows (shear rates, $> 1 \text{ s}^{-1}$) are observed to degrade male-female gamete encounters and consequently fertilization rates [9]. The effects of ambient flow on the flagellar mechanics of sperm motility are not well understood. Here, we focus on elasto-hydrodynamic interactions to elucidate the role of flagellar buckling dynamics in flow and its effect on cell motility.

Sperm are propelled by the propagation of bending waves along their active, elastic eukaryotic flagella [11–13]. The flagella are comprised of a highly-conserved axoneme structure, which usually has nine doublets of parallel microtubules arranged around the periphery of the flagellum and one central pair of microtubules [14–17]. Dynein motors, distributed along the length of the elas-

tic microtubules, create internal shear and thus bending of the axoneme [18]. In a quiescent fluid environment, many sperm exhibit a planar or slightly helicoid flagellar beat pattern resulting in straight [19–21] and helical [19, 21, 22] swimming paths, respectively, where the latter stems from rolling about their longitudinal axis. Asymmetric flagellar waveforms also commonly occur in sperm [19, 23–25], due to either intrinsic factors (elastic instabilities [26], geometrical asymmetry, etc) or external factors (flagellar response to chemical stimuli [2, 27]). The hydrodynamic interactions of sperm with boundaries and other sperm cells are also known to alter flagellar beating, which can ultimately affect sperm swimming trajectories [28–30].

Despite their vast biological and ecological importance [31–35], the mechanics of active flagella in external flows have received markedly less investigation, in comparison to idealized passive elastica and polymers. The buckling and morphological transitions of free elastic filaments have been extensively studied in shear [36, 37] and cellular flows [38, 39]. While flagellar buckling instabilities of sperm due to internal forcing have been reported by theoretical models [26], buckling due to external flow has not. Importantly, this work and others have helped to overcome early modeling limitations for active flagella - including small amplitude beating, infinite length, and prescribed kinematics [11, 13, 40, 41] - by considering the flagellum as an active elastic element [42] and using slen-

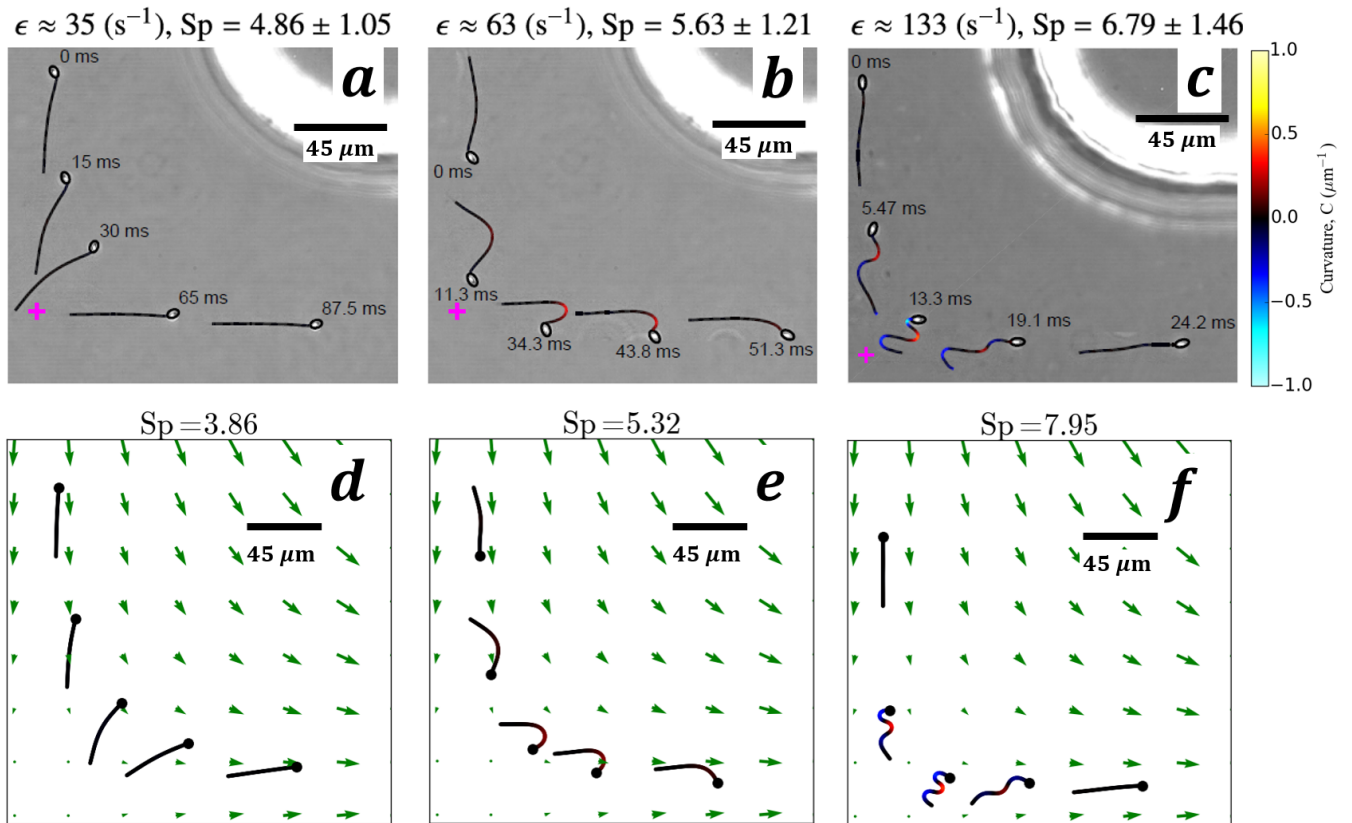


FIG. 1. Top row: Time series overlay of non-motile sperm flagella under varying strain rates from high-speed imaging experiments. The extensional flow is generated using a microfluidic cross channel device, where the magenta plus-sign indicates the location of the hyperbolic point in the extensional flow. Flagellar color represents the measured curvature. Bottom row: Sperm flagellar shapes obtained from numerical simulation under similar conditions to the above experiments. The vector field indicates the extensional flow used in the model.

der body theory to evaluate the hydrodynamic forces [43]. Additionally, many theoretical and numerical studies of stiff polymer [44–48] and flagellar dynamics [26, 42, 49–58] have leveraged Resistive Force Theory (RFT) to successfully approximate hydrodynamic forces [46, 47, 49], when hydrodynamic interactions due to finite filament curvature, neighboring filaments, and walls are not important. Furthermore, RFT reduces the complications of elastic and hydrodynamic interactions while maintaining the reasonable accuracy. Experimentally, the studies of flagella in flow have typically been relegated to simple, uniform flows and artificially immobilized cells using micropipettes [59–61]. Taken together, these studies illustrate that the effect of complex flow on the active flagellar beating and swimming trajectories of sperm cells are poorly explored.

In the present study, we use numerical simulations informed by high-speed imaging experiments to study the buckling dynamics of both passive and active flagella of marine invertebrate sperm in the presence of a non-trivial background flow. At the minute scale of single sperm cells, the complex flow fields present in marine systems can be decomposed into canonical linear flows,

where extensional (and compressional) flow components are primarily responsible for elasto-hydrodynamic interactions. Non-motile marine invertebrate (sea urchin, *Arbacia punctulata*) sperm were subjected to precisely controlled microfluidic extensional flows, where high-speed imaging revealed the onset of flagellar buckling with increasing strain rate (Fig. 1). Modeling the sperm flagellum as an active elastic filament, numerical simulations accurately capture these observations and enable us to explore the rich flagellar buckling dynamics of these cells. We find that flagellar buckling occurs beyond a critical sperm number (Sp), a dimensionless parameter representing the ratio of viscous force to elastic force on the flagellum. For non-motile sperm, the buckling mode as well as the maximum curvature during buckling increase as the sperm number increases. The behavior is similar to Euler beam buckling [62], but the sperm head increases the susceptibility of the flagellum to buckling. For motile sperm, we find that not only Sp but also the beating frequency of flagellum influences the maximum curvature of the flagellar waveform.

II. THEORETICAL FRAMEWORK

Using Resistive Force Theory (RFT), we establish the governing equations for the shape dynamics of sperm through a balance of hydrodynamic and elastic forces, and internal force generation [26, 52, 53, 55]. Many experimental observations have revealed that the flagellar waveforms of sperm from numerous organisms are approximately planar [7, 13, 21, 49]. Thus, we consider 2-D planar beating of a cylindrical sperm flagellum of diameter d , where the geometrical parameters of the active sperm flagellum model are detailed in Fig. 2.

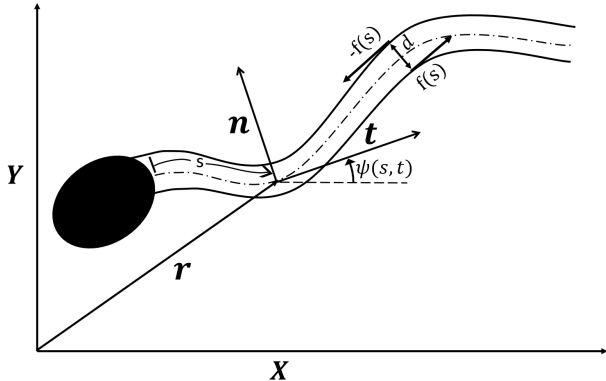


FIG. 2. Schematic of the model sperm geometry, where \mathbf{r} represents the position vector for a point on the centerline of the flagellum. X - Y coordinates denote a fixed frame and s represents the arc-length of flagellum measured from the cell body. Internal shear force field, which generates active flagellar beating, is shown by $f(s, t)$. Unit vectors \mathbf{t} and \mathbf{n} are tangent and normal vectors to the flagellar centerline, respectively. $\psi(s, t)$ is the angle between the tangent vector and the horizontal axis.

In the low Reynolds number approximation, the governing equation for flagellar motion was derived by equating the hydrodynamic force to the elastic force per unit length along the arc-length of the flagellum as (see Fig. 2):

$$(\xi_{\parallel} \mathbf{t}\mathbf{t} + \xi_{\perp} \mathbf{n}\mathbf{n}) \cdot \left\{ \frac{\partial \mathbf{r}}{\partial t} - \mathbf{U} \right\} = -\frac{\delta G}{\delta \mathbf{r}}, \quad (1)$$

where the flagellum has a total arclength, L , and ξ_{\parallel} and ξ_{\perp} are tangential and normal resistance coefficients per unit length of the flagellum, respectively. \mathbf{U} is the background flow field taken here to be $\mathbf{U} = \epsilon(\mathbf{X} - \mathbf{Y})$ with strain rate ϵ . The total elastic energy of the flagellum G is comprised of contributions from bending energy, extensional energy, and active energy, where the latter results from dynein motor activity [53]. Therefore, the expression for the total elastic energy of a flagellum is given by:

$$G = \int_0^L \left\{ \frac{\kappa_s C^2}{2} + \Lambda \frac{\partial \mathbf{r}}{\partial s} \cdot \frac{\partial \mathbf{r}}{\partial s} + f \Delta \right\} ds, \quad (2)$$

where κ_s and C are the flagellar bending stiffness and local curvature, respectively. The dynein motors of the flagellar axoneme generate an internal shear force, $f(s, t)$, which creates relative displacement (Δ) between the microtubule doublets and is responsible for the active component of the elastic energy [63–67]. Λ is the tensile stiffness of the flagellum, which is used here as a Lagrange multiplier to enforce an in-extensibility constraint on the flagellum.

The governing equations are non-dimensionalized, using length scale L , time scale ϵ^{-1} , force density scale $\frac{\epsilon \xi_{\perp} L^2}{d}$, and tension scale $\epsilon \xi_{\perp} L^2$, as follows:

$$\begin{aligned} \gamma \ddot{\tau} - (\dot{\psi})^2 \tau + Sp^{-4} \{ (1 + \gamma) \dot{\psi} \ddot{\psi} + \gamma \dot{\psi}^2 \} \\ - \{ \gamma f \ddot{\psi} + (1 + \gamma) \dot{f} \dot{\psi} \} + \left\{ \frac{\partial u}{\partial s} \right\}_{\parallel} = 0, \end{aligned} \quad (3)$$

$$\begin{aligned} \frac{\partial \psi}{\partial t} + Sp^{-4} \{ \ddot{\psi} - \gamma \dot{\psi}^2 \dot{\psi} \} - (1 + \gamma) \dot{\tau} \dot{\psi} \\ - \tau \ddot{\psi} - (\dot{f} - \gamma \dot{\psi}^2 f) - \left\{ \frac{\partial u}{\partial s} \right\}_{\perp} = 0, \end{aligned} \quad (4)$$

where the over dots represent a derivative with respect to the flagellar arc-length, s . The tension profile $\tau(s, t)$ ensures the local in-extensibility constraint of the flagellum, $\frac{\partial \mathbf{r}}{\partial s} \cdot \frac{\partial \mathbf{r}}{\partial s} = 1$, and $\gamma = \frac{\xi_{\perp}}{\xi_{\parallel}}$ is the ratio of normal resistance coefficient to tangential resistance coefficient. The sperm number $Sp = L \left(\frac{\epsilon \xi_{\perp}}{\kappa_s} \right)^{\frac{1}{4}}$ naturally emerges as the ratio of the viscous drag force to elastic force. $\left\{ \frac{\partial u}{\partial s} \right\}_{\parallel}$ and $\left\{ \frac{\partial u}{\partial s} \right\}_{\perp}$ are the tangential and normal components of the background flow-field derivatives along the arc length s , respectively. The sperm number is traditionally based off of the flagellar beat frequency for motile sperm in quiescent fluids [26]. However, we note that the alternate definition used here [39] - based on the strain rate, ϵ - has utility for both active and inactive elastic filaments and focuses on the effect of externally imposed hydrodynamic forces.

The boundary conditions for these equations result from force and torque balances at the proximal and distal ends of the flagellum. The distal end of the sperm flagellum, $s = 1$, is considered free from external forces, \mathbf{F}_{ext} , and torques, T_{ext} , leading to

$$0 = \mathbf{F}_{ext} = (-Sp^{-4} \ddot{\psi} + f) \mathbf{n} + \tau \mathbf{t}, \quad (5)$$

$$0 = T_{ext} = Sp^{-4} \dot{\psi}, \quad (6)$$

The force and torque at the proximal end of the flagellum ($s = 0$) are balanced with the external force and torque due to the presence of the sperm cell body (head), respectively. The drag force on the sperm head is parameterized by the drag coefficient ζ [53]. This additional drag force increases the compressional force on the sperm flagellum, which increases the susceptibility of the flagellum to buckling. The hydrodynamic torque on the sperm

head can be neglected [68], and the proximal end of the flagellum can be considered torque free. The dimensionless form of the boundary conditions at the proximal end of the flagellum are:

$$-\zeta\left(\frac{\partial \mathbf{r}}{\partial t} - \mathbf{U}\right) = \mathbf{F}_{ext} = (Sp^{-4}\ddot{\psi} - f)\mathbf{n} - \tau\mathbf{t}, \quad (7)$$

$$0 = T_{ext} = -Sp^{-4}\dot{\psi} - \int_0^1 f ds. \quad (8)$$

III. MATERIALS AND METHODS

A. Experiments

Sperm from the purple sea urchin, *Arbacia punctulata*, (Marine Biological Laboratory, Woods Hole, MA) were used as model cells in these experiments. The organisms were held in a 15°C artificial seawater (Instant Ocean) aquarium on a 12h/12h light cycle prior to spawning. The sea urchins were spawned by injecting 1.0 mL of 0.5 M potassium chloride into the body cavity, and sperm were collected dry via pipette ([69]). Cells were diluted by a factor of 10^4 in filtered artificial sea water (FASW), and 0.1% bovine serum albumen (BSA) was added to reduce cell sticking to the microfluidic devices. For non-motile sperm assays, the diluted cells were stored at 4°C for 5 days prior to experiments to ensure loss of motility. All experiments were performed at 22°C in FASW. Precisely controlled extensional flows were generated using a 150 μm deep by 150 μm wide microfluidic cross channel. The microfluidic channels were fabricated in polydimethylsiloxane (PDMS) using standard soft-lithography techniques, and a syringe pump (Harvard Apparatus) was used to control the flow rate and consequently strain rate. Sperm flagellar dynamics were imaged at the mid-depth of the microchannel near the hyperbolic point using phase contrast microscopy (20 \times objective, 0.45 NA) on an inverted microscope (Nikon TE-2000U). The fast buckling events were captured using a high-speed camera (Photron Mini-UX100) at frame rates in the range 2,000-10,000 frames/s (100-200 μs exposure time). Sperm cell bodies and flagella were tracked using an in-house MATLAB routine [70] with sub-pixel accuracy. The flagellar shape dynamics were compactly quantified by the local, instantaneous flagellar curvature, $C(s, t) = (\ddot{X}\dot{Y} - \dot{X}\ddot{Y})/(\dot{X}^2 + \dot{Y}^2)^{3/2}$, which was measured from the tracked sperm cells.

B. Sperm parameter estimation

Flagellar dynamics are principally regulated by the sperm number, which spans a wide range due to significant variations in the flagellar length and mechanical properties across species, and variations in the viscosity of the medium, through which sperm swim [71]. Here,

we restrict the scope of our simulations and experiments by focusing specifically on sperm from the sea urchin *A. punctulata*. These sperm cells are broadly representative of those from external fertilizing marine invertebrates, which exhibit a bare axonemal flagellum ($\approx 0.2 \mu\text{m}$ diameter) [72] and swim in sea water environments [15]. The sperm of various sea urchin species have a flagellar bending stiffness in the range, $\kappa_s = 4 - 9.5 \times 10^{-22} \text{ Nm}^2$ [73], length $L = 30 - 45 \mu\text{m}$, and beating frequency $\omega = 20 - 50 \text{ Hz}$ [15, 19]. In marine environments, turbulent dissipation rates vary from $10^{-10} \text{ m}^2/\text{s}^3$ in the abyssal ocean to $10^{-1} \text{ m}^2/\text{s}^3$ in the most active regions [74]. The estimate of strain rates based on turbulent dissipation rates range from $\epsilon = 0 - O(100) \text{ s}^{-1}$. Here, we explore the effects of strain rates in the range $\epsilon = 1 - 300 \text{ s}^{-1}$. These parameters lead to sperm numbers in the range $Sp = 1 - 10$ in a watery medium, when the flagellar drag force is $\xi_{\perp} = 1.4 - 3.4 \times 10^{-3} \text{ Ns/m}^2$. We use the standard resistance coefficient ratio $\gamma = 2$ for numerical simulations [13, 26, 55]. Furthermore, the normalized drag coefficient of the sperm head, $\zeta = 6\pi\eta a/\xi_{\perp}L$, lies in the range $\zeta = 0.16 - 0.24$, where $\eta = 10^{-3} \text{ Ns/m}^2$ is the viscosity of medium, and $a = 1 - 1.5 \mu\text{m}$ is the radius of the sperm head.

The internal shear force field theory within active flagella has successfully explained the flagellar beating of sperm [42, 49, 51-53, 56], but there is limited quantitative understanding of the nature of internal shear forces generated in the axoneme [75]. In the present study, we calculate the internal shear force similar to our previous study [8]. We accomplish this by solving the governing equations (3 and 4) for shear force $f(s, t)$ instead of flagellar shape $\psi(s, t)$ by considering the beating pattern of the sperm flagellum in a quiescent fluid, $\psi_0(s, t)$. We use the mathematical model of the flagellar beating pattern having a traveling wave:

$$\psi_0(s, t) = \cos(2\pi s - \Omega t), \quad (9)$$

which mimics the waveform of sea urchin sperm in a quiescent fluid [4, 8, 76]. $\Omega = \frac{\omega}{\xi}$ is the dimensionless beating frequency of flagellum, where ω is the dimensional beating frequency.

C. Numerical approach

We use a semi-implicit method to solve the nonlinear-coupled governing equations, where only the highest order derivative of each nonlinear term is treated implicitly (t_{n+1}) and the rest are considered at the previous time step (t_n). The flagellar shape was then reconstructed from the local tangent angle $\psi(s, t)$ as $\mathbf{r}(s, t) = \mathbf{r}(0, t) + \int_0^s (\cos(\psi), \sin(\psi)) ds'$, where $\mathbf{r}(0, t)$ has been obtained by evaluating equation 1 at $s = 0$. The details of the numerical approach and the validation of the numerical tool can be found in Kumar and Ardekani [8]. For simulations of sperm in flow, both motile and non-motile sperm are initialized ($t = 0$) upstream of the hyperbolic

point with the center of their head located at $Y = 4.0$. As observed in experiments, the cells are initially parallel to the Y -axis, and we chose their cell body (head) to be oriented away from the hyperbolic point in the upstream direction, unless noted otherwise. We also find that the buckling dynamics of flagella is independent of the head's orientation, whether it is toward or away from the hyperbolic point, as long as the sperm is initially parallel to Y -axis.

IV. RESULTS AND DISCUSSION

To gain insight into the hydrodynamic and elastic forces governing the morphological dynamics of flagella in flow, we first study the buckling of non-motile sperm flagella in an extensional flow through both experiments and numerical simulations. Based on the strong agreement between the model and measurements of non-motile sperm, we extend our studies to also model the dynamics of motile sperm in flow. Throughout the study, we examine the shape dynamics of the sperm flagella as they transiently pass through an extensional flow from the the compressional axis to the extensional axis. During the study, we compactly describe the flagellar shape through a kymograph (time-curvature) plot of normalized curvature, $C(s, t)$, as a function of normalized arc-length s and time t . The variables are normalized using the flagellar length L and the strain rate ϵ , and the curvature is further normalized by the maximal curvature incurred during a buckling event $C(s, t)/C_{\max}$.

A. Buckling of non-motile sperm flagella

The sperm flagellum initially aligns with the compressional axis of the flow upstream of the hyperbolic point, and then it rotates to realign towards the extensional direction downstream of the hyperbolic point due to its Jeffery rotation (supplementary video 2 and video 5 [81]) [77] with minimal bending at small strain rate (Sp). The dynein motors of non-motile sperm do not generate an internal shear force field, and therefore, for the numerical study of non-motile sperm flagella, we assume $f(s, t) = 0$. The simulations capture the Jeffery rotation of cells near the hyperbolic point, where they behave similarly to rigid rods (Fig. 1a and d). Because of their propensity to align along the extensional axes of the flow, the sperm flagellum experiences a compressive force upstream and a tensile force downstream of the hyperbolic point as it aligns with the streamlines. The upstream compressive force leads to buckling of the flagellum for large Sp in both experiments and simulations (see supplementary video 3 and video 6 [81]), and the cells exhibit higher buckling modes with increasing Sp . The spatiotemporal evolution of the flagellum's morphology from numerical simulations is in excellent agreement with high-speed imaging experiments (Fig. 1), encouraging further investigation of the

buckling of non-motile sperm flagella in an extensional flow.

The numerical simulations (Fig. 3b and f) capture the buckling dynamics observed in high-speed imaging experiments (Fig. 3a and e), which we visualize through time-curvature plots of the sperm flagellum. At low Sp , a transient buckling event with a single buckling location appears as a region of high curvature (Fig. 3a,b), which unfurls and moves toward the sperm head as the cell transits through the hyperbolic point before straightening due to hydrodynamic extension of the flagellum. At higher extension rates, and thus Sp , higher buckling modes are accessed, for example with three locations of large magnitude alternating curvature (Fig. 3e,f). As the buckled flagellar shape evolves, the alternating curvature regions annihilate one another or are unstretched in the extensional region of the flow. The numerical simulations are exploited to probe yet higher sperm numbers, where the time-curvature plots depicted in Fig. 3 show that the number of locations where buckling occurs (i.e. buckling mode), increases with increasing Sp . The buckling dynamics become increasingly complex at large Sp , where some high curvature regions persists and others rapidly annihilate (Fig. 3h).

To quantify the degree of buckling, we calculate the maximum absolute curvature (C_{\max}) of the flagellum during buckling (Fig. 4). Unlike large sperm numbers, at small sperm number buckling does not occur, and the flagellum remains straight with $C_{\max} < 1$. For a head drag coefficient of $\zeta = 0.2$, we observe a critical onset of buckling at $Sp_{\text{cr}} \approx 3.8$, beyond which C_{\max} rapidly increases. We use $|C| = 0.3$, which is the value of C_{\max} at Sp_{cr} , as a cut off curvature to identify the buckling modes. Without the sperm head, the critical buckling threshold determined from our simulations was found to increase to $Sp_{\text{cr}} \approx 4.26$, which is in agreement with the analytic prediction of Young and Shelley [38] for elastic fibers in the hyperbolic flow (see Appendix A). As the strain rate increases, Sp increases and leads to an enhanced compressive force acting on the flagellum, therefore, the number of buckling locations (mode) increases with Sp . In the absence of head, a non-motile flagellum behaves as an elastic filament and the transition of buckling mode of the flagellum can be explained using eigenvalues of an elastic fiber as discussed in earlier works [38, 78]. Eigenvalues of a free filament in an extensional flow is characterized by alternating odd and even dominant modes. The sperm number, at which the dominant eigenmode switches from even (odd) to odd (even) [38, 78], is the sperm number whereat the transition of the buckling mode of the flagellum occurs (Appendix A). As expected, the additional hydrodynamic drag due to the presence of the sperm head reduces the value of sperm numbers at which buckling modes change (Fig. 4). Regardless of the number of buckling locations, the maximum curvature of the flagellum monotonically increases as a function of Sp with few exceptions. These exceptions correspond to the transitions between buck-

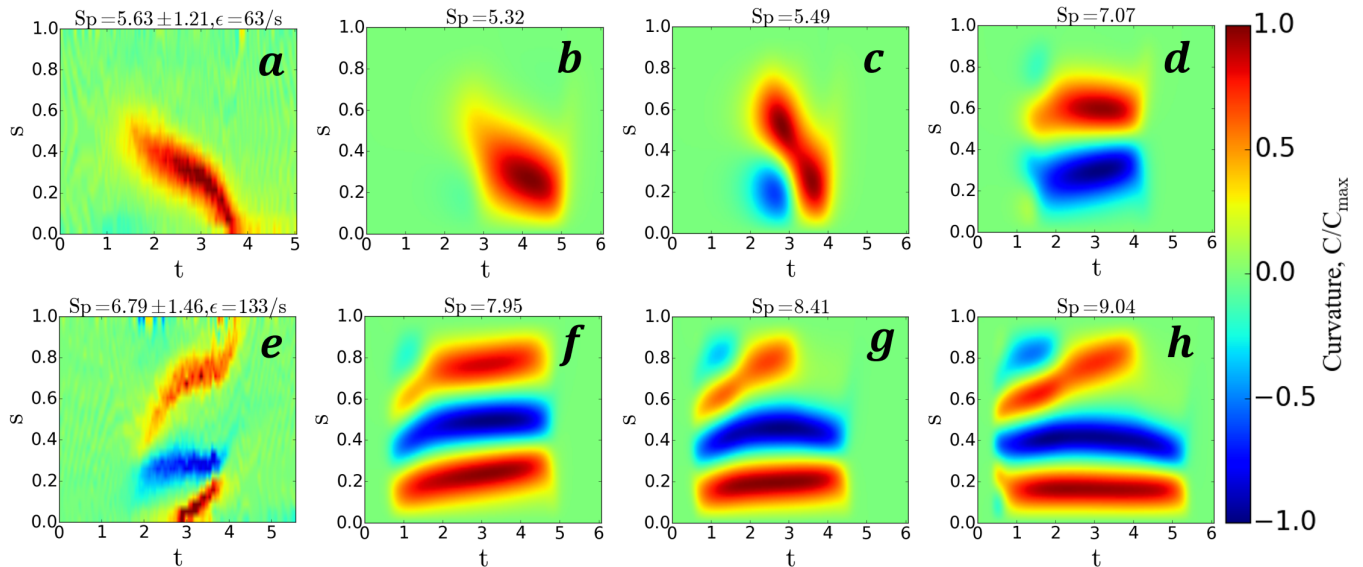


FIG. 3. Time-curvature plots of non-motile sperm flagella in an extensional flow. Panels (a) and (e) are the time-curvature plots of flagellar buckling obtained from experiments, and correspond to the flagellar shapes shown in Fig. 1b and c. The remaining plots are time-curvature plots obtained from numerical simulations for a given Sp .

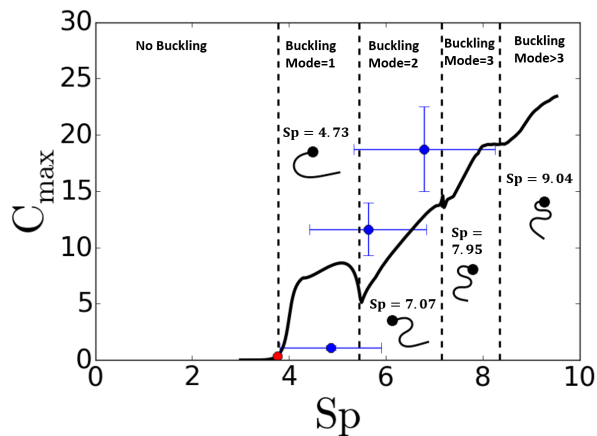


FIG. 4. The maximum absolute curvature of the flagellum at different Sp . Red solid circle is the critical $Sp_{cr} \approx 3.8$ required for flagellar buckling. Dotted vertical lines separate the region of different buckling modes determined by identifying the buckling locations with $|C| > 0.3$ in the time-curvature plots. Blue solid circle is the C_{max} of flagellum obtained from experiments and correspond to Fig. 1a, b and c. The small schematics of sperm represent the shape of the flagellum, when the maximum curvature occurs for a given Sp .

ling modes (see Fig. 4). Due to the non-linearity of the governing equations, we observe a range of Sp within which the transition of buckling mode completes. Fig. 3c shows a time-curvature plot during the transition from the first to the second buckling mode. For the first buckling mode, the flagellum buckles in only one region and does not exhibit a counter-bend. Therefore, the maxi-

mum curvature decreases with Sp during the transition from the first to the second buckling mode, $Sp=5.10-5.49$ (Fig. 4).

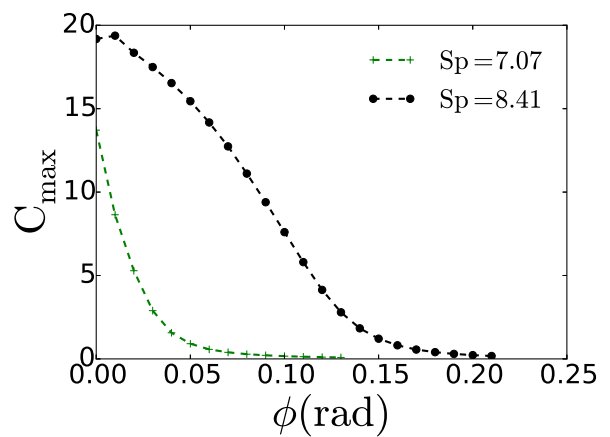


FIG. 5. The maximum absolute curvature decreases with initial misalignment of the flagellum from the upstream compressional axis for different Sp .

In naturally occurring unsteady and chaotic flows, elongated cells and particles are not necessarily aligned to the compressional axis when entering a hyperbolic point [79]. Thus, we also numerically study the effect of an initial misalignment of the flagellum with the upstream flow direction on flagellar buckling (Fig. 5). The maximum buckling curvature of the sperm flagellum is highly dependent on the initial alignment angle, $\phi (< \pi/2)$, of the flagellum with the local streamline. The compressive hydrodynamic force acting on the flagellum decreases as the

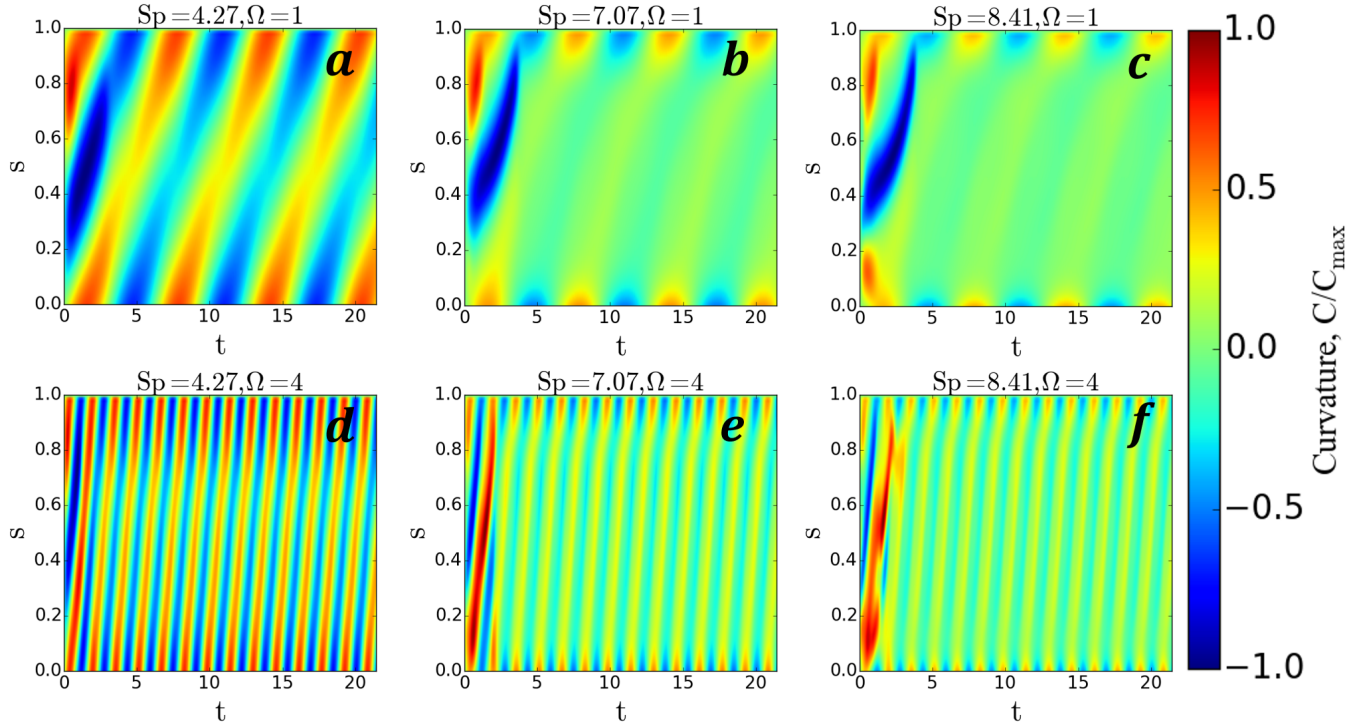


FIG. 6. Time-curvature plot of numerically simulated motile sperm flagellar dynamics in an extensional flow. The internal driving shear force, $f(s, t)$, was obtained from a mathematically modeled symmetric flagellar beating pattern, $\psi_0(s, t) = \cos(2\pi s - \Omega t)$, in a quiescent fluid. Sp is constant in each column and beating frequency (Ω) is constant in each row.

angle between the flagellar orientation and the incident streamline increases, which leads to a rapid decrease of the maximum curvature of the flagellum with misalignment angle ϕ . At smaller Sp , C_{\max} decreases with ϕ more rapidly, and the buckling of the flagellum disappears at large ϕ (Fig. 5). As expected, the minimum value of ϕ beyond which flagellar buckling disappears increases with increasing Sp . The time interval, within which the flagellum remains buckled, also decreases as the misalignment angle (ϕ) increases, because the flagellum is required to rotate by a smaller angle to align with the downstream extensional axis (see Appendix B). While the maximum curvature of the flagellum is a strong function of its initial orientation, the number of buckling locations is independent of the misalignment angle, ϕ (Appendix B).

B. Buckling dynamics of motile sperm flagella

In contrast to non-motile sperm, actively beating flagella induce local curvature changes for cell propulsion through internal dynein motor activity. We study the effect of preexisting curvature during flagellar beating on the buckling dynamics of sperm flagella and motility. Fig. 6 depicts time-curvature plots for a model sperm flagellum in the presence of an extensional flow. Here, a mathematically modeled symmetric flagellar beating pattern (Eq. 9) has been used to obtain the internal driving shear

force, $f(s, t)$, within the flagellum in a quiescent fluid (supplementary video 1 [81]). At small sperm numbers, the flagellum doesn't buckle and the beating pattern remains symmetric (first column of Fig. 6). Above a critical Sp_{cr} , the flagellum buckles, and the beating pattern becomes asymmetric (supplementary video 4 [81]). We find that the critical Sp_{cr} for motile sperm flagellar buckling is the same as for non-motile sperm. The motile sperm flagellum has predilection for instantaneous buckling locations due to the preexisting curvature (Appendix C). Notably, the upstream compressive force of the extensional flow only enlarges the curvature without creating new buckling points at larger Sp . Therefore, the number of points where buckling occurs does not depend on Sp for motile sperm. Fig. 6 shows that the flagellar waveform becomes uniform after some time and the variation of curvature decreases with increasing Sp . During upstream compression, the sperm buckles and rotates, which leads to realignment of the flagellum with the streamlines in the downstream flow direction. The flagellum experiences downstream tensile forces of the extensional flow causing the beating pattern of the flagellum to return to a symmetric waveform.

To elucidate changes in the sperm flagellar beating pattern during a transit through the extensional flows studied here, we examine the instantaneous flagellar shape and compare it to an unperturbed, symmetric flagellar waveform for a sperm occurring at the same head loca-

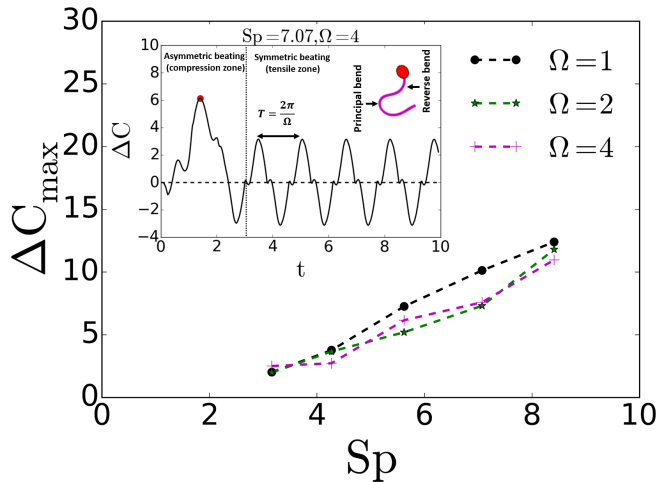


FIG. 7. The instantaneous difference between the maximum curvature of principal and reverse bend (ΔC) vs time (inset). The maximum value of ΔC at different Sp and Ω . This value corresponds to red solid circle in the inset.

tion and shear angle (supplementary video 4 [81]). The deviation of the flagellar waveform from the symmetric beating pattern in the upstream zone occurs due to buckling under compressive hydrodynamic forces. We have also plotted the instantaneous difference between the maximum curvature of principal and reverse bend ($\Delta C(t) = C_{\text{principal,max}} - C_{\text{reverse,max}}$) in the inset of Fig. 7. Principal bend is the bend which has maximum absolute curvature (C_{max}) during the buckling. A cartoon explaining principal bend and reverse bend has been depicted in the inset of Fig. 7. In the compressional zone, flagellar beating becomes asymmetric and the degree of asymmetry (ΔC_{max}) increases with Sp (Fig. 7). In contrast, the beating pattern remains symmetric in the tensile zone as indicated by the mirror symmetry of ΔC after a half beating period (i.e., $\Delta C(t) = -\Delta C(t + T/2)$) (see inset of Fig. 7) [78]. The external tensile hydrodynamic forces compete with internal bending to strongly reduce the beating amplitude, which is indicated by a sharp decrease in the ratio of the flagellar beating amplitude in the tensile region of the flow normalized by the beating amplitude in a quiescent fluid (Fig. 8). We also observe that the reduction in the beating amplitude of the flagellum is larger at smaller beating frequencies. Higher flagellar beat frequencies have stronger internal force generation. Therefore, the cells with higher beat frequency are more difficult to deform by external forces.

Furthermore, we investigated the effects of Sp and beating frequency (Ω) on the maximum curvature of the flagellum (Fig. 9). Beyond the critical Sp_{cr} , the upstream compressive force enhances the maximum curvature (C_{max}) of the flagellum through buckling. The strength of the compressive force increases with Sp , leading to an amplification of the existing maximum flagellar curvature (Fig. 9). Similar to supplementary video 4

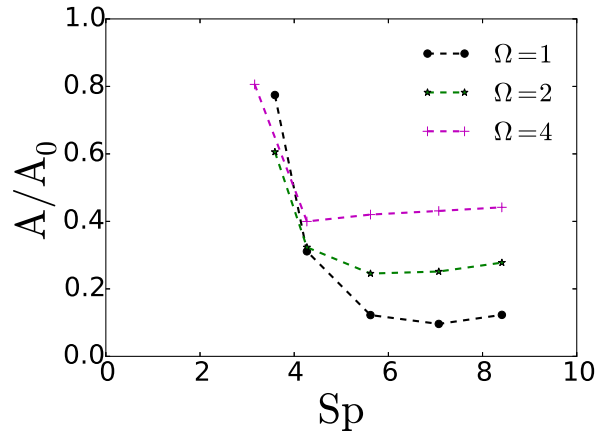


FIG. 8. The ratio of flagellar beating amplitude in the tensile zone of the extensional flow to the flagellar beating amplitude in the quiescent fluid vs Sp at different beating frequencies.

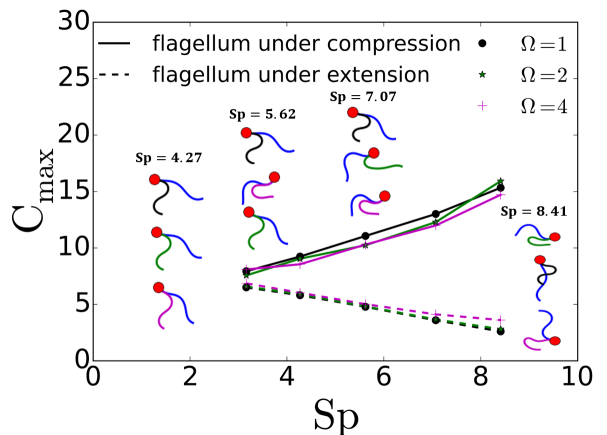


FIG. 9. The maximum curvature of the sperm flagellum, having $f(s, t)$ obtained from a mathematical model of the waveform, at different Sp and flagellar beating frequencies (Ω) in the upstream (compressional) zone as well as downstream (tensile) zone of the extensional flow. The small schematics of sperm (except blue) depict the shape of the sperm flagellum, when the maximum curvature occurs during the compression of the flagella. The schematics colored blue represent the shape of flagellum having symmetric beating.

[81], the schematics of beating sperm flagella are shown in Fig. 9 for when C_{max} occurs in the compressional zone and compared to a symmetric beating pattern (colored blue). This illustration further shows the asymmetric flagellar conformations of the buckled flagellum in the upstream region. In a similar manner to the non-motile cells, the intensity of the compressive hydrodynamic force also depends on the sperm orientation with respect to the streamlines, where the flagellum experiences maximum compression when the sperm is oriented parallel to streamlines. For a given Sp , the maximum curvature at different beating frequencies does not occur for the

same orientation of sperm. Therefore, the beating frequency, for which the sperm's angle with the streamlines is smaller, gives larger C_{\max} (see sperm schematics in Fig. 9). In the downstream extensional zone, the curvature at the end of the flagellum is only slightly affected by the tensile force (Fig. 6). Therefore, we consider only the interior portion of the flagellum ($s = 0.1 - 0.9$) to calculate C_{\max} in the tensile (downstream) regime. In addition to reducing the beating amplitude, the tensile force incurred by the sperm in the downstream region also reduces the maximal curvature of the flagellum with increasing Sp . Collectively, these simulations show that the flagellar motility of sperm is hampered by strong external flows. While fluid advection and rotation can sweep swimming cells off course, buckling in the compressive upstream regime results in asymmetric beating that can further rotate cell orientation, and reduced beating amplitude in the tensile downstream region results in less effectual swimming.

V. CONCLUSIONS

Spermatozoa from diverse species of both external and internal fertilizing organisms interact with dynamic fluid flows during the fertilization process. Focusing on marine invertebrate sperm (sea urchin, *A. punctulata*), we illustrate how local hyperbolic regions of flow dictate the elasto-hydrodynamics of passive and active flagella, principally through extensional and compressional stresses. Combining numerical modeling with high-speed video and microfluidic experiments, we show that the sperm flagellum experiences a compressive force upstream in a background extensional flow and a tensile force downstream, which dictate the buckling and stretching of flagella, respectively. The dimensionless sperm number (Sp), representing the ratio of viscous force to elastic force, characterizes the influence of the strain rate on flagellar dynamics, where sperm flagella are observed to buckle beyond a critical Sp_{cr} . The flagellar buckling dynamics are sensitive to the orientation of sperm relative to the compressional axis, which could play an important role in the manifestation of flagellar buckling in unsteady and turbulent environmental flows. The absolute maximum curvature (C_{\max}) of the flagellum characterizes the degree of buckling, which increases with Sp for both motile and non-motile sperm. The number of buckling locations along the flagellum (buckling mode) increases with increasing strain rate for non-motile sperm, similar to Euler buckling modes in elastic rods [62].

Strikingly, for motile sperm, the inherent flagellar curvature acts as a precursor for buckling, where the number of buckling locations is preserved. Flagellar buckling in the compressional zone induces asymmetric beating of the flagellum, whereas flagellar beating remains symmetric in the tensile zone. Internal flagellar forces amplify the buckling intensity in the upstream region, while tensile forces downstream resist flagellar actuation

forces [26] and thus flagellar buckling. In sum, the results presented here illustrate potential mechanisms, such as flagellar buckling and stretching, that can impact sperm cell mechanics and motility in flow. Motility is a crucial component of the fertilization process for both marine invertebrate and mammalian sperm, which utilize a bevy of environmental cues, most notably chemotaxis [1, 2, 4, 9], to navigate toward female gametes for reproduction. However, our understanding of how flagellar elasto-hydrodynamics in flow affect the active flagellar turning motility associated with sperm chemotactic navigation [2], and thus the sperm-egg fertilization [9], remains an open question.

VI. APPENDIX

A. Buckling mode of non-motile flagellum

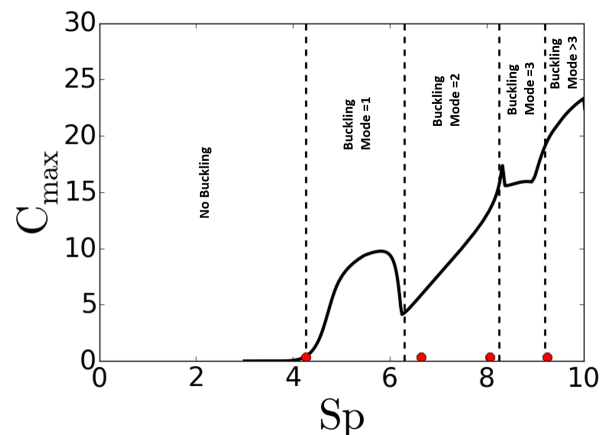


FIG. 10. The maximum curvature of the simulated flagellum during buckling in the absence of sperm head (solid black curve). Dotted vertical lines separate Sp regimes of different buckling modes determined by identifying the buckling locations with $|C| > 0.3$ in the time-curvature plots. Red solid circles are the theoretically predicted Sp in the literature [38, 78] for the transition of buckling modes of an elastic filament through a linear analysis. In the absence of a sperm cell body (head), the critical Sp of the flagellar buckling was found to be the same as the theoretical prediction for an elastic fiber, $Sp_{cr} = 4.26$.

While theoretical analysis of the sperm flagellar buckling dynamics for the full cell structure, including the cell body and flagellum, are challenging, we can compare our simulation results to previous work on the dynamics of elastic filaments in flow [38, 78]. Elimination of the sperm head from our simulations reveals that the onset of buckling increases from $Sp_{cr} \approx 3.8$ (Fig. 4) to $Sp_{cr} \approx 4.26$, as determined from the maximum curvature (Fig. 10). The transition for the first buckling mode strongly agrees with previous theoretical analyses for Sp_{cr} for an elastic filament [38], determined by linear analysis. The observed

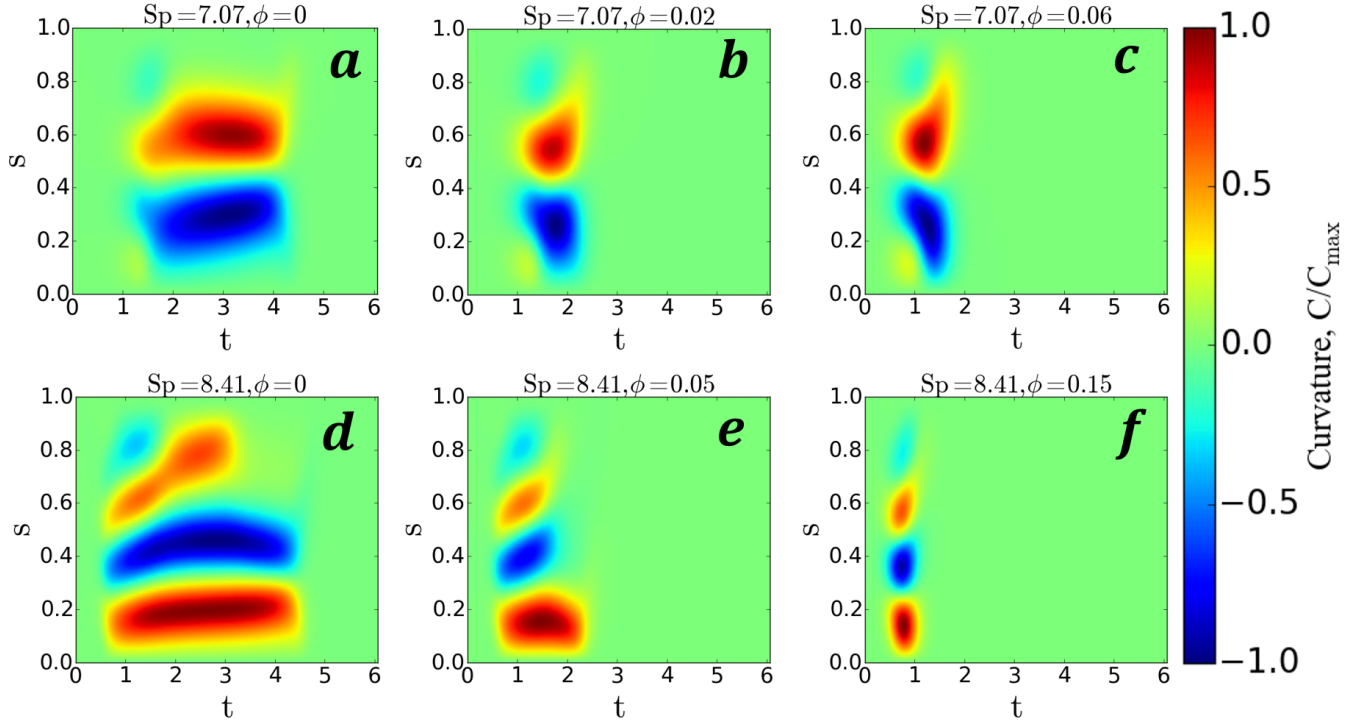


FIG. 11. Time-curvature plot of non-motile sperm flagella for different initial misalignment angles ϕ . Sp is constant in each row.

transitions for higher buckling modes are similarly shifted to higher Sp in comparison to the full sperm model including the head and tail. The transitions are determined by identifying the buckling locations with $|C| > 0.3$ in the time-curvature plots and show good agreement with theory [38, 78]. The sperm number required for the transition of buckling mode of the flagellum is equivalent to the sperm number required to switch the dominant eigenmode in the eigenvalues diagram of filament (Fig. 10).

B. Effect of initial misalignment on buckling

The degree of buckling is strongly affected by the initial misalignment angle of nonmotile sperm flagella with the upstream compressive axis of the flow. While transiting through the hyperbolic point, the sperm rotates by a smaller angle to align with the downstream streamlines of the extensional region as the initial misalignment angle (ϕ) of flagellum increases. This feature reduces the time duration and thus severity of buckling events as ϕ increases (Fig. 11).

C. Location of instantaneous C_{\max} in the motile sperm flagellum

The instantaneous location along the flagellum of motile sperm, where maximum curvature occurs in the

presence of compressional flow, is approximately the same as the location of maximum curvature in a quiescent fluid at that instant (Fig. 12).

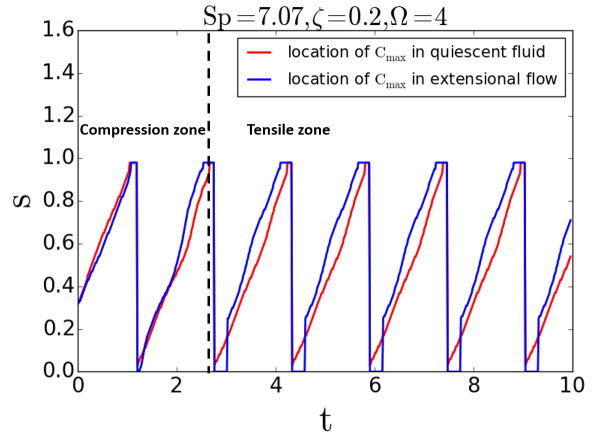


FIG. 12. The location of the instantaneous maximum flagellar curvature in the presence of extensional flow compared to that in a quiescent fluid for the simulations shown in supplementary video 4 [81].

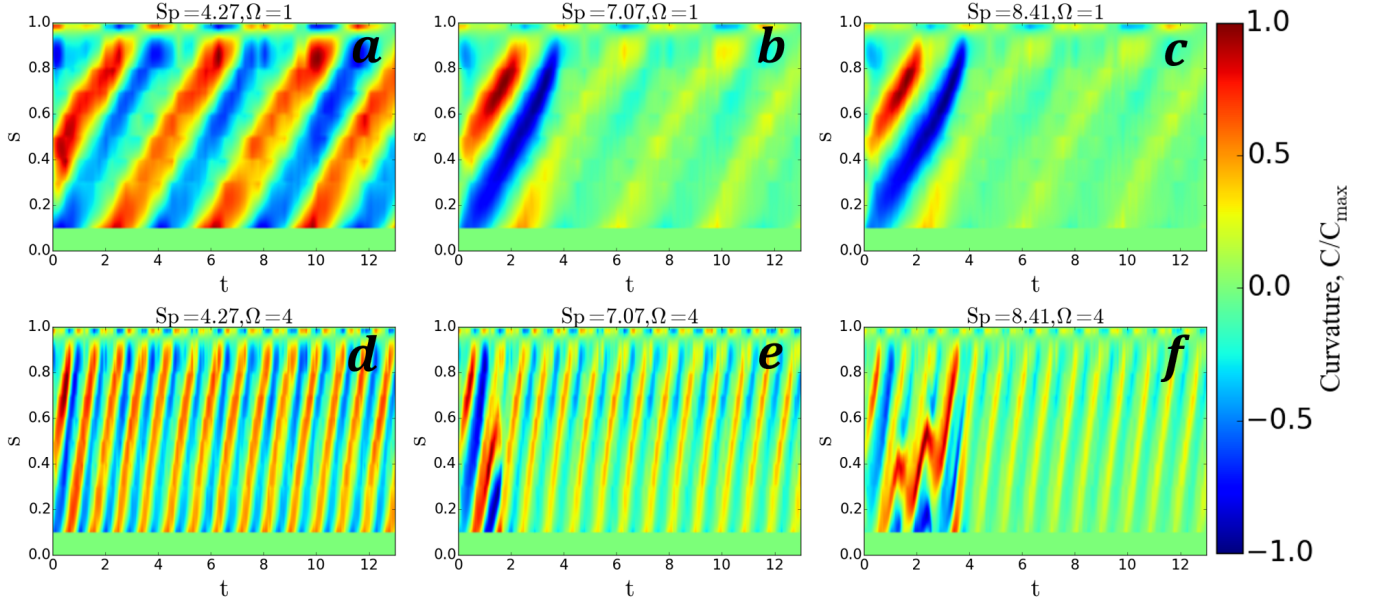


FIG. 13. Time-curvature plots of numerically modeled motile sperm flagella, for which $f(s, t)$ has been obtained directly from high-speed imaging experiments, in an extensional flow at different Sp and beating frequencies. The flow doesn't significantly affect the curvature close to the proximal end of flagellum. Therefore, we omit data close to head.

D. Integrated buckling simulations with experimentally measured flagellar waveforms

Here, we utilize high-speed imaging experiments of flagellar waveform of actively swimming sea urchin sperm (*A. punctulata*) in quiescent fluid to directly extract the internal shear forcing. Using a hybrid computational and experimental approach, the internal forcing generated by a flagellum is computed from measured flagellar kinematics using our numerical framework. Flagellar waveforms from motile sperm, measured as described above (750 frames/s) in a quiescent observation chamber, were utilized in buckling simulations to provide realistic flagellar dynamics. Briefly, a set of curvature basis modes, $u_i(s)$, [80] were extracted from several thousand measured flagellar waveforms comprising four individual cells using a singular value decomposition (SVD) algorithm in MATLAB. The two highest energy modes captured $\approx 92\%$ of the flagellar shape. The curvature of the flagellum was obtained by the linear combination of two highest energy modes, $C(s, t) = a_1(t)u_1(s) + a_2(t)u_2(s)$, where $a_1(t)$ and $a_2(t)$ are periodic mode amplitude functions. While the flagellar beat parameters and mechanical properties of the live sperm are largely fixed, we explore a range of different Sp and Ω by artificially rescaling the experimentally measured cell kinematics for the purposes of the model. In this way, we use the data to obtain $f(s, t)$ for different flagellar beating frequencies.

Fig. 13 shows the numerically computed flagellar time-curvature plots for motile sperm in an extensional flow at different Sp and beating frequencies. Here, $f(s, t)$ has been extracted directly from experimentally measured

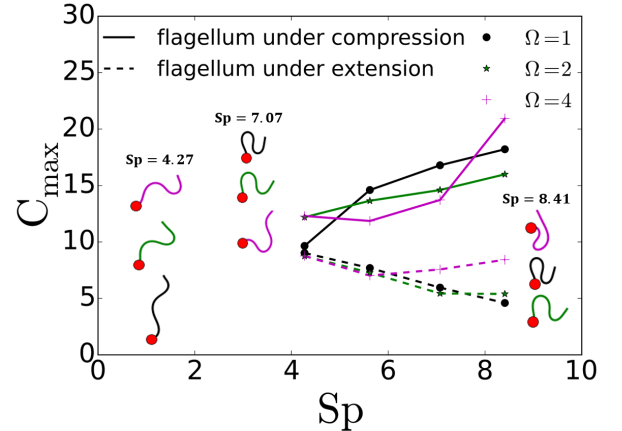


FIG. 14. The maximum curvature of sperm flagella, having $f(s, t)$ obtained directly from experimentally measured flagellar waveforms for sea urchin sperm (*A. punctulata*), at different Sp and synthetic flagellar beating frequencies (Ω) in the upstream (compressional) zone and downstream (tensile) zone of the extensional flow. The small schematics of sperm depict the shape of the sperm flagellum, when the maximum curvature occurs during the compression of the flagella.

flagellar waveforms, yet the flagellar curvatures show strikingly similar dynamics to the properties of the mathematically modeled sperm flagellar beating (see Fig. 6 in the main text). Likewise, we examine the maximal curvature C_{\max} of the sperm flagella from experimentally extracted flagellar waveforms in the upstream (compressional) as well as downstream (tensile) zones of the

extensional flow (Fig. 14). The maximal flagellar curvature, C_{\max} , for the experimentally extracted flagellar waveform (Fig. 14) mirrors the behavior of the mathematically modeled sperm results (Fig. 9 in the main text), whereby C_{\max} increases with Sp in the compressional region and decays with Sp in the extensional region.

VII. ACKNOWLEDGEMENT

We thank Roman Stocker and Gabriel Juarez for discussions on early experimental work, and we acknowl-

edge funding from National Science Foundation awards CBET-1700961 (to A.M.A.), and CBET-1701392 and CAREER-1554095 (to J.S.G.).

-
- [1] U. B. Kaupp, N. D. Kashikar, and I. Weyand, Mechanisms of Sperm Chemotaxis, *Annual Review of Physiology* **70**, 93 (2008).
- [2] M. Spehr, G. Gisselmann, A. Poplawski, J. A. Riffell, C. H. Wetzel, R. K. Zimmer, and H. Hatt, Identification of a testicular odorant receptor mediating human sperm chemotaxis, *Science* **299**, 2054 (2003).
- [3] R. K. Zimmer and J. A. Riffell, Sperm chemotaxis, fluid shear, and the evolution of sexual reproduction, *Proceedings of the National Academy of Sciences* **108**, 13200 (2011).
- [4] J. F. Jikeli, L. Alvarez, B. M. Friedrich, L. G. Wilson, R. Pascal, R. Colin, M. Pichlo, A. Rennhack, C. Brenker, and U. B. Kaupp, Sperm navigation along helical paths in 3D chemoattractant landscapes, *Nature Communications* **6**, 10.1038/ncomms8985 (2015).
- [5] K. Miki and D. E. Clapham, Article Rheotaxis Guides Mammalian Sperm, *Current Biology* **23**, 443 (2013).
- [6] V. Kantsler, J. Dunkel, M. Blayney, and R. E. Goldstein, Rheotaxis facilitates upstream navigation of mammalian sperm cells, *eLife* **3**, 1 (2014).
- [7] A. Bukatin, I. Kukhtevich, N. Stoop, J. Dunkel, and V. Kantsler, Bimodal rheotactic behavior reflects flagellar beat asymmetry in human sperm cells, *Proceedings of the National Academy of Sciences* **112**, 15904 (2015).
- [8] M. Kumar and A. M. Ardekani, Effect of external shear flow on sperm motility, *Soft Matter* , 13 (2019).
- [9] J. A. Riffell and R. K. Zimmer, Sex and flow: the consequences of fluid shear for sperm egg interactions, *Journal of Experimental Biology* **210**, 3644 (2007).
- [10] J. P. Crimaldi and R. K. Zimmer, The Physics of Broadcast Spawning in Benthic Invertebrates, *Annual Review of Marine Science* **6**, 141 (2014).
- [11] G. Taylor, Analysis of the Swimming of Microscopic Organisms, *Proceedings of the Royal Society A: Mathematical, Physical and Engineering Sciences* **209**, 447 (1951).
- [12] G. J. Hancock, The Self-Propulsion of Microscopic Organisms through Liquids, *Proceedings of the Royal Society A: Mathematical, Physical and Engineering Sciences* **217**, 96 (1953).
- [13] J. Gray and G. J. Hancock, The Propulsion of Sea-Urchin Spermatozoa, *Journal of Experimental Biology* **32**, 802 (1955).
- [14] B. Afzelius, Electron Microscopy of the Sperm Tail Results Obtained with a New Fixative, *The Journal of Cell Biology* **5**, 269 (1959).
- [15] C. Brennen and H. Winet, Fluid Mechanics of Propulsion by Cilia and Flagella, *Annual Review of Fluid Mechanics* **9**, 339 (1977).
- [16] D. W. Fawcett, A Comparative View of Sperm Ultrastructure1, *Biology of Reproduction* **2**, 90 (1970).
- [17] G. E. Olson and R. W. Linck, Observations of the structural components of flagellar axonemes and central pair microtubules from rat sperm, *Journal of Ultrastructure Research* **61**, 21 (1977).
- [18] D. Nicastro, The Molecular Architecture of Axonemes Revealed by Cryoelectron Tomography, *Science* **313**, 944 (2006).
- [19] B. Y. J. Gray, THE MOVEMENT OF SEA-URCHIN SPERMATOOZOA, (1955).
- [20] D. F. Katz, E. Z. Drobnis, and J. W. Overstreet, Factors regulating mammalian sperm migration through the female reproductive tract and oocyte vestements, *Gamete Research* **22**, 443 (1989).
- [21] D. J. Smith, E. A. Gaffney, H. Gadelha, N. Kapur, and J. C. Kirkman-Brown, Bend propagation in the flagella of migrating human sperm, and Its modulation by viscosity, *Cell Motility and the Cytoskeleton* **66**, 220 (2009).
- [22] A. T. Chwang, T. Y. Wu, and J. Gray, A note on the helical movement of micro-organisms, *Proceedings of the Royal Society of London. Series B. Biological Sciences* **178**, 327 (1971).
- [23] R. Rikmenspoel, Biophysical approaches to the measurement of sperm motility, *Spermatozoan Motility*. Washington: American Association for the Advancement of Science , 31 (1962).
- [24] D. M. Phillips, Comparative analysis of mammalian sperm motility **53**, 10.1083/jcb.53.2.561 (1972).
- [25] G. David, C. Serres, and P. Jouannet, Kinematics of Human Spermatozoa, **95**, 83 (1981).
- [26] H. Gad elha, E. A. Gaffney, D. J. Smith, and J. C. Kirkman-Brown, Nonlinear instability in flagellar dynamics: A novel modulation mechanism in sperm migration?, *Journal of the Royal Society Interface* **7**, 1689 (2010).
- [27] B. Y. R. L. Miller and C. J. Brokaw, Chemotactic turning behaviour of Tubularia spermatozoa, , 699 (1970).
- [28] L. J. Fauci and A. McDonald, Sperm motility in the presence of boundaries, *Bulletin of Mathematical Biology* **57**, 679 (1995).

- [29] H. Winet, G. S. Bernstein, and J. Head, Observations on the response of human spermatozoa to gravity, boundaries and fluid shear, *Reproduction* **70**, 511 (1984).
- [30] D. M. Woolley, Motility of spermatozoa at surfaces, *Reproduction* **126**, 259 (2003).
- [31] F. Azam, T. Fenchel, J. Field, J. Gray, L. Meyer-Reil, and F. Thingstad, The Ecological Role of Water-Column Microbes in the Sea, *Marine Ecology Progress Series* **10**, 257 (1983).
- [32] D. L. Kirchman, New light on an important microbe in the ocean, *Proceedings of the National Academy of Sciences* **105**, 8487 (2008).
- [33] L. J. Fauci and R. Dillon, Biofluidmechanics of Reproduction, *Annual Review of Fluid Mechanics* **38**, 371 (2006).
- [34] E. Lauga and T. R. Powers, The hydrodynamics of swimming microorganisms, *Reports on Progress in Physics* **72**, 096601 (2009).
- [35] J. S. Guasto, R. Rusconi, and R. Stocker, Fluid Mechanics of Planktonic Microorganisms, *Annual Review of Fluid Mechanics* **44**, 373 (2011).
- [36] L. E. Becker and M. J. Shelley, Instability of elastic filaments in shear flow yields first-normal-stress differences, *Physical Review Letters* **87**, 198301 (2001).
- [37] Y. Liu, B. Chakrabarti, D. Saintillan, and A. Lindner, Morphological transitions of elastic filaments in shear flow, **115**, 9438 (2018).
- [38] Y. Young and M. J. Shelley, Stretch-Coil Transition and Transport of Fibers in Cellular Flows, **058303**, 3 (2007).
- [39] E. Wandersman, N. Quennouz, M. Fermigier, A. Lindner, and O. Roure, Buckled in translation , , 5715 (2010).
- [40] G. Taylor, Analysis of the Swimming of Long and Narrow Animals, *Proceedings of the Royal Society A: Mathematical, Physical and Engineering Sciences* **214**, 158 (1952).
- [41] J. Shen, P. Tam, W. Shack, and T. Lardner, Large amplitude motion of self-propelling slender filaments at low Reynolds numbers, *Journal of Biomechanics* **8**, 229 (1975).
- [42] K. E. Machin, Wave propagation along flagella, *The Journal of experimental biology* **35**, 796 (1958).
- [43] R. G. Cox, The motion of long slender bodies in a viscous fluid Part 1. General theory, *Journal of Fluid Mechanics* **44**, 791 (1970).
- [44] R. E. Goldstein and S. A. Langer, Nonlinear Dynamics of Stiff Polymers, *Physical Review Letters* **75**, 1094 (1995).
- [45] C. H. Wiggins and R. E. Goldstein, Flexive and Propulsive Dynamics of Elastica at Low Reynolds Number, *Physical Review Letters* **80**, 3879 (1998).
- [46] C. H. Wiggins, D. Riveline, A. Ott, and R. E. Goldstein, Trapping and Wiggling: Elastohydrodynamics of Driven Microfilaments, *Biophysical Journal* **74**, 1043 (1998).
- [47] T. S. Yu, E. Lauga, and A. E. Hosoi, Experimental investigations of elastic tail propulsion at low Reynolds number, *Physics of Fluids* **18**, 1 (2006).
- [48] L. Bourdieu, T. Duke, M. B. Elowitz, D. A. Winkelmann, S. Leibler, and A. Libchaber, Spiral defects in motility assays: A measure of motor protein force, *Physical Review Letters* **75**, 176 (1995).
- [49] I. H. Riedel-Kruse and A. Hilfinger, How molecular motors shape the flagellar beat, *HFSP Journal* **10.2976/1.2773861** (2007).
- [50] C. J. Brokaw, Non-sinusoidal bending waves of sperm flagella., *The Journal of experimental biology* **43**, 155 (1965).
- [51] C. J. Brokaw, Bend propagation by a sliding filament model for flagella., *The Journal of experimental biology* **55**, 289 (1971).
- [52] S. Camalet, F. Jülicher, and J. Prost, Self-Organized Beating and Swimming of Internally Driven Filaments, *Physical Review Letters* **82**, 1590 (1999).
- [53] S. Camalet and F. Jülicher, Generic aspects of axonemal beating, *New Journal of Physics* **2**, 24 (2000).
- [54] H. C. Fu, C. W. Wolgemuth, and T. R. Powers, Beating patterns of filaments in viscoelastic fluids, *Physical Review E - Statistical, Nonlinear, and Soft Matter Physics* **78**, 1 (2008).
- [55] A. Hilfinger, A. K. Chattopadhyay, and F. Jülicher, Non-linear dynamics of cilia and flagella, *Physical Review E* **79**, 051918 (2009).
- [56] M. Hines and J. J. Blum, Bend propagation in flagella. I. Derivation of equations of motion and their simulation, *Biophysical Journal* **23**, 41 (1978).
- [57] A. Hilfinger and F. Jülicher, The chirality of ciliary beats, *Physical Biology* **5**, 10.1088/1478-3975/5/1/016003 (2008).
- [58] B. M. Friedrich, I. H. Riedel-Kruse, J. Howard, and F. Jülicher, High-precision tracking of sperm swimming fine structure provides strong test of resistive force theory, *Journal of Experimental Biology* **213**, 1226 (2010).
- [59] G. Quaranta, M. E. Aubin-Tam, and D. Tam, Hydrodynamics Versus Intracellular Coupling in the Synchronization of Eukaryotic Flagella, *Physical Review Letters* **115**, 1 (2015).
- [60] G. S. Klindt, C. Ruloff, C. Wagner, and B. M. Friedrich, Load Response of the Flagellar Beat, *Physical Review Letters* **117**, 1 (2016).
- [61] C. Shingyoji, I. R. Gibbons, A. Murakami, and K. Takahashi, Effect of imposed head vibration on the stability and waveform of flagellar beating in sea urchin spermatozoa., *J. Exp. Biol.* **156**, 63 (1991).
- [62] S. P. Timoshenko, *Theory of Elastic Stability* (Dover Publications, Newburyport :, 2009).
- [63] C. Brokaw, Direct measurements of sliding between outer doublet microtubules in swimming sperm flagella, *Science* **243**, 1593 (1989).
- [64] K. E. Summers and I. R. Gibbons, Adenosine triphosphate-induced sliding of tubules in trypsin-treated flagella of sea-urchin sperm (motility/microtubule/cilia/sliding filament model/axonemes), *Proceedings of the National Academy of Science* **68**, 3092 (1971).
- [65] I. R. Gibbons and A. J. Rowe, Dynein: A Protein with Adenosine Triphosphatase Activity from Cilia, *Science* **149**, 424 (1965).
- [66] M. E. Porter and W. S. Sale, The 9 + 2 axoneme anchors multiple inner arm dyneins and a network of kinases and phosphatases that control motility, *Journal of Cell Biology* **151**, 37 (2000).
- [67] G. G. Vernon and D. M. Woolley, Microtubule displacements at the tips of living flagella, *Cell Motility and the Cytoskeleton* **52**, 151 (2002).
- [68] K. Ishimoto and E. A. Gaffney, Fluid flow and sperm guidance: a simulation study of hydrodynamic sperm rheotaxis, *Journal of The Royal Society Interface* **12**, 20150172 (2015).
- [69] L. Alvarez, L. Dai, B. M. Friedrich, N. D. Kashikar, I. Gregor, R. Pascal, and U. B. Kaupp, The rate of change in Ca²⁺ concentration controls sperm chemotaxis, *Jour-*

- nal of Cell Biology **196**, 653 (2012).
- [70] C. P. Brangwynne, G. H. Koenderink, E. Barry, Z. Dogic, F. C. MacKintosh, and D. A. Weitz, Bending Dynamics of Fluctuating Biopolymers Probed by Automated High-Resolution Filament Tracking, *Biophysical Journal* **93**, 346 (2007).
- [71] H. Gadêlha and E. A. Gaffney, Flagellar ultrastructure suppresses buckling instabilities and enables mammalian sperm navigation in high-viscosity media, *Journal of The Royal Society Interface* **16**, 20180668 (2019).
- [72] C. K. Omoto and C. J. Brokaw, Structure and behaviour of the sperm terminal filament, *J Cell Sci* **58**, 385 (1982).
- [73] D. W. Pelle, C. J. Brokaw, K. A. Lesich, and C. B. Lindemann, Mechanical properties of the passive sea urchin sperm flagellum, *Cell Motility and the Cytoskeleton* **66**, 721 (2009).
- [74] S. A. O. Thorpe, *The turbulent ocean /* (Cambridge University Press, Cambridge ;, 2005).
- [75] E. Gaffney, H. Gadêlha, D. Smith, J. Blake, and J. Kirkman-Brown, Mammalian Sperm Motility: Observation and Theory, *Annual Review of Fluid Mechanics* **43**, 501 (2011).
- [76] R. Rikmenspoel, Movement of sea urchin sperm flagella, *The Journal of Cell Biology* **76**, 310 (1978).
- [77] G. B. Jeffery, The Motion of Ellipsoidal Particles Immersed in a Viscous Fluid, *Proceedings of the Royal Society A: Mathematical, Physical and Engineering Sciences* **102**, 161 (1922).
- [78] L. Guglielmini, A. Kushwaha, E. S. G. Shaqfeh, and H. A. Stone, Buckling transitions of an elastic filament in a viscous stagnation point flow, *Physics of Fluids* **24**, 10.1063/1.4771606 (2012).
- [79] S. Parsa, J. S. Guasto, M. Kishore, N. T. Ouellette, J. P. Gollub, and G. A. Voth, Rotation and alignment of rods in two-dimensional chaotic flow, *Physics of Fluids* **23**, 10.1063/1.3570526 (2011).
- [80] Guglielmo Saggiorato, Luis Alvarez, Jan F. Jikeli, U. Benjamin Kaupp, Gerhard Gompper, and Jens Elgeti. Human sperm steer with second harmonics of the flagellar beat, *Nature Communications*, 8(1), 2017.
- [81] See Supplementary Material at [url will be inserted by publisher] for movies of sperm motion in an extensinal flow at different Sp.